Resonant third-generation leptoquark signatures at the Large Hadron Collider

Ulrich Haisch[1] and Giacomo Polesello[2]

[1]*Max Planck Institute for Physics, Föhringer Ring 6, 80805 München, Germany*
[2]*INFN, Sezione di Pavia, Via Bassi 6, 27100 Pavia, Italy*

E-mail: haisch@mpp.mpg.de, giacomo.polesello@cern.ch

ABSTRACT: Given the hints of lepton-flavour non-universality in B-meson decays, leptoquarks (LQs) are enjoying a renaissance. We propose novel Large Hadron Collider (LHC) searches for such hypothetical states that do not rely on strong production only, but can also receive important contributions from quark-lepton annihilation. For the cases of a resonant signal involving a bottom quark and a tau lepton ($b + \tau$), a top quark and missing transverse energy (E_T^{miss}) and light-flavour jets plus E_T^{miss}, we develop realistic analysis strategies and provide detailed evaluations of the achievable sensitivities for the corresponding LQ signatures at future LHC runs. Our analyses allow us to derive a series of stringent constraints on the masses and couplings of third-generation singlet vector LQs, showing that at LHC Run III and the high-luminosity LHC the proposed search channels can probe interesting parts of the LQ parameter space addressing the B-physics anomalies. In view of the reach of the proposed $b + \tau$ signature, we recommend that dedicated resonance searches for this final state should be added to the exotics search canon of both ATLAS and CMS.

Contents

1   Introduction

The deviations from τ-μ (and τ-e) universality in $b \rightarrow c\ell\nu$ transitions [1–6] and the deviations from μ-e universality in $b \rightarrow s\ell^+\ell^-$ transitions [7, 8] are commonly considered the most compelling departures from the Standard Model (SM) observed by collider experiments in recent years. As a result of a significant amount of theoretical work [9–38] it is by now well-established that singlet vector leptoquarks (LQs) with a mass in the TeV range and third-generation couplings provide a simple, especially appealing explanation of both sets of anomalies.

Several different search strategies for third-generation LQs have so far been considered at the Large Hadron Collider (LHC). While the ATLAS and the CMS collaborations have mainly focused on LQ pair production via strong interactions in gluon-gluon fusion or quark-antiquark annihilation (cf. [39–43] for the latest results), the importance of LQ pair production via t-channel exchange of a lepton, of LQ exchange in Drell-Yan (DY) like di-lepton production and of single LQ production in gluon-quark fusion in constraining the quark-lepton-LQ couplings has also been established [28, 29, 44–57].

Due to quantum fluctuations, protons however also contain charged leptons, making it is possible to target lepton-induced processes at the LHC as well. The simplest process of this kind consists in the collision between a quark from one proton and a lepton from the other proton, giving rise to resonant single LQ production at hadron colliders [58]. In fact, using the precise determination of the lepton parton distribution functions (PDFs) obtained recently in [59], it has been shown in [60] that LHC searches for s-channel single LQ production provide the strongest constraints to date on all the flavour combinations of first- and second-generation minimal scalar

LQs that involve an up or a down quark. Given the suppression of the relevant quark PDFs, the constraints on minimal scalar LQ interactions involving a strange or a charm quark turn out to be less stringent but still relevant in view of the large amount of data collected in the high-luminosity era of the LHC (HL-LHC).

The main goal of this article is to extend and generalise the basic ideas and results presented in the publication [60] (see subsequently also [61]) to the case of singlet vector LQs, coupled mainly to third-generation fermions. To this purpose, we develop three search strategies for LQ signatures that are induced by quark-lepton annihilation at the LHC. The first search strategy exploits final states with a bottom quark (b) and a tau lepton (τ), while the second and third search strategy targets final states with a single top quark (t) and significant amounts of missing transverse energy (E_T^{miss}) and light-flavour jets (j) plus E_T^{miss}, respectively. In all three cases we provide detailed evaluations of the achievable sensitivities for the LQ signature at LHC Run III and the HL-LHC. These sensitivities are then used to constrain singlet vector LQ models with left- as well as third-generation right-handed quark-lepton-LQ couplings and/or sizeable second-third-generation left-handed mixing. LQ scenarios of this kind have also been considered in the recent detailed collider analysis [53]. We will benchmark the bounds derived in our work against the limits obtained in the latter study.

The remainder of this article is organised as follows. In Section 2 we briefly describe the structure of the LQ model that we consider, while we explain in Section 3 which resonant LQ production channels are particularly motivated by the B-physics anomalies. The main ingredients of our Monte Carlo (MC) generation and our detector simulation are discussed in Section 4. The actual analysis strategies are detailed in Section 5. In Section 6 we present our numerical results and examine the sensitivity of the studied LQ signatures at upcoming LHC runs. We conclude and present an outlook in Section 7.

2 Theoretical framework

In this article, we consider a LQ called U that transforms as $(\mathbf{3}, \mathbf{1})_{2/3}$ under the SM gauge group $SU(3)_c \times SU(2)_L \times U(1)_Y$. Such a LQ can either appear as a massive gauge boson of a spontaneously broken gauge symmetry [17–24, 27, 30, 32] or arise as a massive vector resonance of some new strongly-interacting dynamics [12, 15, 16, 34]. Irrespectively of its ultraviolet (UV) origin, the quantum numbers of U unambiguously fix the quark-lepton-LQ interactions to have the form

$$\mathcal{L} \supset \frac{g_U}{\sqrt{2}} \left[\beta_L^{ij} \, \bar{Q}_L^{i,a} \gamma_\mu L_L^j + \beta_R^{ij} \, \bar{d}_R^{i,a} \gamma_\mu \ell_R^j \right] U^{\mu,a} \; + \text{h.c.} \,, \tag{2.1}$$

where, without loss of generality, the down-type quark and charged-lepton mass eigenstate basis has been adopted for the left-handed fermion multiplets:

$$Q_L^i = \begin{pmatrix} V_{ji}^* u_L^j \\ d_L^i \end{pmatrix}, \qquad L_L^i = \begin{pmatrix} \nu_L^i \\ \ell_L^i \end{pmatrix}. \tag{2.2}$$

In (2.1) and (2.2) the elements of the Cabibbo-Kobayashi-Maskawa (CKM) matrix are denoted by V_{ij}, the fields d_R (ℓ_R) represent the right-handed down-type quark (charged-lepton) singlets, $i, j \in \{1, 2, 3\}$ are flavour indices, $a \in \{1, 2, 3\}$ is a colour index, g_U denotes the overall coupling strength of the quark-lepton-LQ interactions, and $\beta_{L,R}^{ij}$ are complex 3×3 matrices in flavour space.

Parameters			Branching ratios			
β_L^{33}	β_L^{23}	β_R^{33}	$\mathrm{BR}\,(U \to b\tau^+)$	$\mathrm{BR}\,(U \to t\bar{\nu}_\tau)$	$\mathrm{BR}\,(U \to s\tau^+)$	$\mathrm{BR}\,(U \to c\bar{\nu}_\tau)$
1	0	0	51%	49%	0%	0%
1	1	0	25%	22%	25%	27%
1	0	1	68%	32%	0%	0%

Table 1. Branching ratios of U for $M_U = 1\,\mathrm{TeV}$ and three different choices of $\beta_L^{33}, \beta_L^{23}$ and β_R^{33}.

The latest global analyses (see for instance [31, 32, 53]) of lepton-flavour universality (LFU) violation in charged-current $b \to c$ transitions (i.e. $R_{D^{(*)}}$) and in neutral-current $b \to s$ transitions (i.e. $R_{K^{(*)}}$) show that a singlet vector LQ with a mass $M_U = \mathcal{O}(1\,\mathrm{TeV})$ and a coupling $g_U = \mathcal{O}(1)$ provides an excellent description of the B anomalies if the left-handed quark-lepton-LQ couplings entering (2.1) have the following hierarchy:

$$\left|\beta_L^{22}\right| \lesssim \left|\beta_L^{32}\right| \ll \left|\beta_L^{23}\right| \lesssim \left|\beta_L^{33}\right| = \mathcal{O}(1)\,. \tag{2.3}$$

While there is no clear indication of right-handed currents in present B-meson data, motivated UV completions of (2.1) such as those proposed in [20, 24, 32] give rise to:

$$\left|\beta_R^{33}\right| = \mathcal{O}(1)\,. \tag{2.4}$$

In order to restrict the number of model parameters we furthermore assume that all quark-electron-LQ couplings vanish, and that $\beta_L^{13} = V_{td}^*/V_{ts}^* \beta_L^{23} \simeq -\lambda \beta_L^{23}$ as in models [12, 16, 20, 21, 23, 24, 27, 32, 53] based on a minimal breaking of the assumed $U(2)_Q$ flavour symmetry of first- and second-generation quarks. Here $\lambda \simeq 0.2$ denotes the Cabibbo angle. Both assumptions are phenomenologically well-motivated given the tight constraints from low-energy measurements, in particular the bounds on lepton-flavour violation in charged-lepton decays and the limits on neutral meson mixing (see e.g. [16, 24, 32]).

3 Resonant LQ signals motivated by B anomalies

The discussion in the previous section should have made clear that in the singlet vector LQ model a successful explanation of the B-physics anomalies relies largely on the five variables

$$M_U\,, \qquad g_U\,, \qquad \beta_L^{33}\,, \qquad \beta_L^{23}\,, \qquad \beta_R^{33}\,, \tag{3.1}$$

while the left-handed couplings β_L^{32} and β_L^{22} represent only small perturbations needed to accommodate the deviations observed in the $b \to s$ sector. Hereafter we will therefore focus on the subset (3.1) of model parameters, setting the left-handed couplings β_L^{32} and β_L^{22} as well as all right-handed couplings other than β_R^{33} to zero.

In the limit of $M_U \gg m_f$ with m_f denoting the masses of the SM fermions and working to leading order in the Cabibbo angle, the tree-level expressions of the relevant partial decay widths
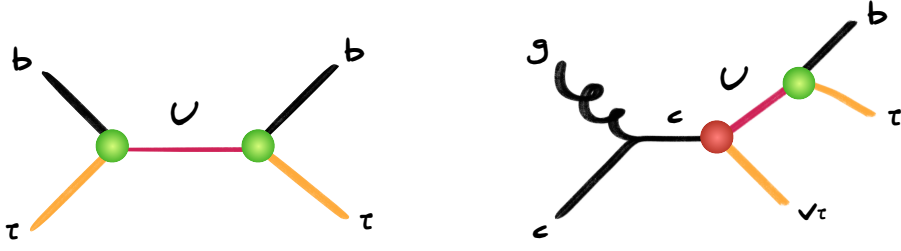
Figure 1.   Examples of tree-level Feynman diagrams giving rise to a final state involving a b quark and a τ lepton. The green vertices indicate the couplings β_L^{33} or β_R^{33}, while the red vertex corresponds to β_L^{23}. Graphs with t-channel exchange of a U also contribute to $b\tau \to b\tau$ scattering if $\beta_L^{33} \neq 0$ or $\beta_R^{33} \neq 0$, while the s-channel process $s\tau \to b\tau$ is also possible if $\beta_L^{23} \neq 0$. Diagrams corresponding to the latter two $2 \to 2$ transitions are not depicted. In the case of the $2 \to 3$ process also diagrams with t-channel exchange of a U and graphs involving a gluon-LQ-LQ vertex contribute to the shown $gc \to b\tau\nu_\tau$ reaction. These contributions have again not been displayed. For further details consult the main text.

of the singlet vector LQ read

$$\Gamma\left(U \to b\tau^+\right) \simeq \frac{g_U^2}{48\pi}\left(\left|\beta_L^{33}\right|^2 + \left|\beta_R^{33}\right|^2\right)M_U\,, \qquad \Gamma\left(U \to t\bar{\nu}_\tau\right) \simeq \frac{g_U^2}{48\pi}\left|\beta_L^{33}\right|^2 M_U\,,$$

$$\Gamma\left(U \to s\tau^+\right) \simeq \frac{g_U^2}{48\pi}\left|\beta_L^{23}\right|^2 M_U\,, \qquad\qquad \Gamma\left(U \to c\bar{\nu}_\tau\right) \simeq \frac{g_U^2}{48\pi}\left|\beta_L^{23}\right|^2 M_U\,. \tag{3.2}$$

In Table 1 we report the corresponding branching ratios of U for $M_U = 1\,\mathrm{TeV}$ and three different choices of the parameters β_L^{33}, β_L^{23} and β_R^{33} — notice that due to phase-space and quark-mixing effects the shown branching ratios deviate slightly from the values expected from (3.2). From the above formulas one observes that for fixed β_L^{33} increasing β_L^{23} increases the $j + E_T^{\mathrm{miss}}$ (i.e. mono-jet) signal strength relative to $b+\tau$ and $t + E_T^{\mathrm{miss}}$ (i.e. mono-top) and vice versa. Varying the coupling β_R^{33} instead allows to change the importance of the $b + \tau$ final state relative to the $t + E_T^{\mathrm{miss}}$ and $j + E_T^{\mathrm{miss}}$ final states with larger (smaller) values of β_R^{33} enhancing (decreasing) the $b + \tau$ branching ratio.

The relative magnitudes of the couplings $\beta_L^{33}, \beta_L^{23}$ and β_R^{33} do not only dictate the decay pattern of the singlet vector LQ, but also determine how the U is produced. This feature is illustrated in Figure 1, which shows examples of tree-level diagrams leading to resonant single U production via bottom-tau annihilation (left) and single U production in gluon-charm annihilation (right) followed by the decay $U \to b\tau$. Hereafter we will for simplicity often refer to the two different production mechanisms as the $2 \to 2$ and the $2 \to 3$ process, respectively. As indicated in the figure by the coloured vertices for $\beta_L^{33} \neq 0$ or $\beta_R^{33} \neq 0$ the process $b\tau \to U \to b\tau$ takes place even if $\beta_L^{23} = 0$, while the rate for $gc \to U\nu_\tau \to b\tau\nu_\tau$ is non-zero only if $\beta_L^{23} \neq 0$. In fact, in view of (2.3) and (2.4) one expects that singlet vector LQ model realisations that provide an explanation of the $R_{D^{(*)}}$ anomalies feature resonant $b + \tau$ and mono-top production in bottom-tau annihilation at the LHC. Mono-jet production via $b\tau \to c\nu_\tau$ or $s\tau \to c\nu_\tau$ is also possible but requires the second-third-generation left-handed mixing parameter β_L^{23} to be sufficiently large.

The above discussion of the decay pattern and the production mechanisms of U singles out the $b + \tau$, $t + E_T^{\text{miss}}$ and $j + E_T^{\text{miss}}$ final states as the most promising resonant production channels to search for the presence of a singlet vector LQ as motivated by the $b \to c\,(s)$ anomalies. Other important search channels for third-generation singlet vector LQs are pair production leading to $b\bar{b}\tau^+\tau^-$ and $t\bar{t}\nu_\tau\bar{\nu}_\tau$ final states, DY-like $\tau^+\tau^-$ (i.e. di-tau) production as well as $\tau\nu_\mu$ and $\tau\mu$ production through t-channel exchange of a U — for a comprehensive analysis of these final states see [53]. In the following, we will concentrate on the $b + \tau$, mono-top and mono-jet signatures because the LHC sensitivity of these channels to the five-dimensional parameter space (3.1) has not yet been studied.

4 MC generation and detector simulation

The signal predictions are calculated at leading order (LO) using the implementation [53] of the Lagrangian (2.1) together with the `LUXlep` PDFs, which have been obtained by combining the lepton PDFs of [59] with the `NNPDF3.1luxQED` set [62]. The generation and showering of the LQ samples is performed with `MadGraph5_aMCNLO` [63] and `PYTHIA 8.2` [64], respectively. Since `PYTHIA 8.2` presently cannot deal with incoming leptons, all initial state leptons (i.e. e, μ and τ) have been replaced by photons in the Les Houches files before showering the events. Our signal simulations therefore do not include leptons but quarks arising from photon splitting in the parton shower (PS) backward evolution. We expect the resulting mismodelling of the hadronic and leptonic activity of the LQ signals to have only a very minor impact on the numerical results obtained below in Section 6.

In the case of the $b + \tau$ and the mono-top signature all SM processes that contain one or two charged leptons from the decay of a electroweak (EW) gauge boson $V = W, Z$ or the decay of a τ lepton are included in the background. The generation of the relevant $b + \tau$ and mono-top backgrounds follows [65]. Specifically, the backgrounds from $t\bar{t}$ [66], tW [67], WW, WZ and ZZ production [68, 69] are generated at next-to-leading order (NLO) in QCD with `POWHEG BOX` [70]. The V + jets backgrounds are generated at LO using `MadGraph5_aMC@NLO` and include up to four additional jets. The $t\bar{t}V$ backgrounds are also simulated at LO with `MadGraph5_aMC@NLO` and include up to two additional jets, while the tZ and tWZ backgrounds are obtained at LO with the same MC generator. The production of $b + \tau$ from an initial-state bottom quark and a tau lepton via t-channel exchange of a photon or Z boson also represents an irreducible background. We include this background at LO using `MadGraph5_aMC@NLO`. All partonic events are showered with `PYTHIA 8.2`. The samples produced with `POWHEG BOX` are normalised to the corresponding NLO QCD cross sections, except for $t\bar{t}$ which is normalised to the cross section obtained at next-to-next-to-leading order (NNLO) in QCD plus next-to-next-to-leading logarithmic QCD corrections [71, 72]. The V + jets samples are normalised to the NNLO QCD cross sections [73, 74] and the $t\bar{t}V$ samples are normalised to the NLO QCD cross section as calculated by `MadGraph5_aMC@NLO`.

For the mono-jet signature, the dominant SM backgrounds arise from V + jets production. The only relevant process not included in the one-lepton backgrounds described above is the Z + jets channel followed by the decay $Z \to \nu\bar{\nu}$. Like in our earlier work [75] it is generated at LO with `MadGraph5_aMC@NLO`, and can contain up to two additional jets. The generation is performed in slices of the vector-boson p_T, and the resulting events are showered with `PYTHIA 8.2` employing

a Catani-Krauss-Kuhn-Webber jet-matching procedure [76]. The inclusive signal region IM3 of the analysis [77] requires $E_T^{\mathrm{miss}} > 350\,\mathrm{GeV}$, and for these selections the background from $V +$ jets production amounts to around 95% of the total SM background. Our $V +$ jets samples are normalised such that the different contributions match the number of events in the IM3 signal region as estimated by the ATLAS collaboration scaled to a centre-of-mass (CM) energy of 14 TeV and to the appropriate integrated luminosity. The additional minor backgrounds from $t\bar{t}$, tW and diboson production are the same as in the $b + \tau$ and the mono-top case.

Electrons and muons produced in the decays of real EW gauge bosons and taus that are isolated from jets are considered in our analyses. Jets are built out of the moments of all the stable particles depositing energy in the calorimeter except for muons using the anti-k_t algorithm [78] with a radius parameter of $R = 0.4$, as implemented in FastJet [79]. Jets originating from the hadronisation of bottom quarks (b-jets) and the hadronic decays of τ leptons are experimentally identified (i.e. tagged) with high efficiency. The $\vec{p}_T^{\,\mathrm{miss}}$ vector with magnitude E_T^{miss} is constructed from the transverse momenta of all the invisible particles in the event. The experimental effects are simulated by smearing the momenta of the analysis objects and by applying efficiency factors where applicable. The used smearing and efficiency functions are tuned to reproduce the performance of the ATLAS detector [80, 81]. In particular, the performance of the ATLAS b-tagging algorithm is taken from [82]. For the analyses performed in this article, a b-tagging working point is chosen that yields a b-tagging efficiency of 77%, a c-jet rejection of 5 and a light-flavour jet rejection of 110. The parametrisation of the τ-tagging performance is taken from [83]. The used τ-tagging working point has an average efficiency of approximately 80% and 70% for the identification of tau leptons in hadronic decays into a single charge particle (one-prong decays) and into three charged particles (three-prong decays), respectively. The assumed rejection factor for light-flavour jets is taken to be 80 (500) for hadronic one-prong (three-prong) tau decays.

5 Analysis strategies

In this section we detail our analysis strategies that are designed to target the $b + \tau$, mono-top and mono-jet final states. For each analysis strategy we spell out all selection criteria and illustrate their impact on the SM background and the LQ distributions of interest.

5.1 $b + \tau$ final state

The basic selection for the $b + \tau$ signature consists of a b-tagged hadronic jet (b) and a hadronic jet corresponding to the hadronic decay of a tau lepton (τ_{had}). We require $p_T(b) > 50\,\mathrm{GeV}$ and $p_T(\tau_{\mathrm{had}}) > 150\,\mathrm{GeV}$, where the latter requirement is dictated by the expected trigger thresholds for the single τ trigger at the HL-LHC [83]. Both the b-jet and the τ_{had} are required to be within $|\eta| < 2.5$, which is the pseudorapidity coverage of the ATLAS tracker. We further veto events with additional jets tagged as a b or a τ, or any additional light-flavour jet with $p_T > 50\,\mathrm{GeV}$. Moreover all events containing a reconstructed light lepton (e or μ) are discarded. Besides a b-jet and a τ_{had}, the $b + \tau$ signal also comprises E_T^{miss} associated to neutrinos. Notice that these neutrinos can either result from the τ decay itself or from associated production depending on whether the $2 \rightarrow 2$ or the $2 \rightarrow 3$ process is considered (see Figure 1). Since the $2 \rightarrow 2$ and the $2 \rightarrow 3$ processes lead to final states with very different kinematic features, it is essential to develop two separate strategies
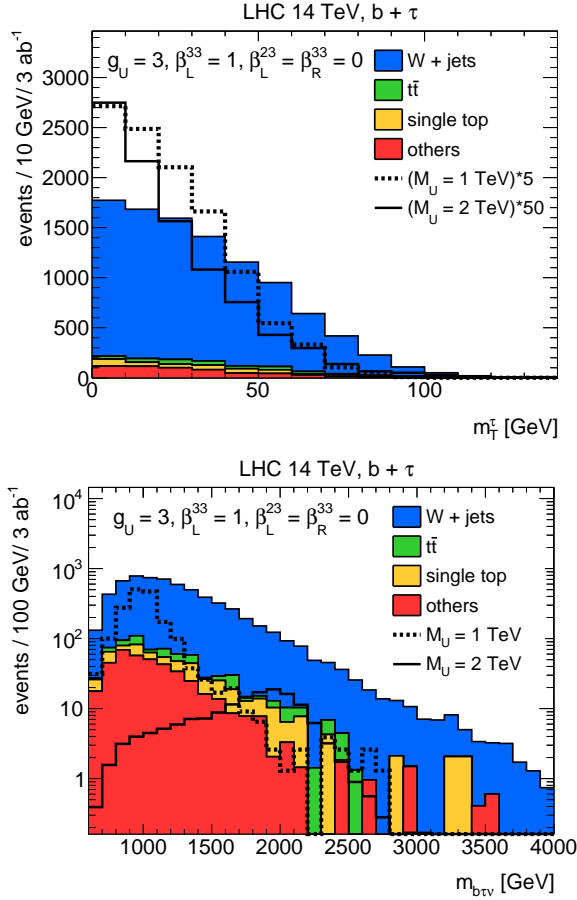
Figure 2. Upper panel: m_T^τ distribution for the background and two $b + \tau$ signals scaled up by a factor of 5 and 50, respectively. Lower panel: $m_{b\tau\nu}$ distribution for the background and two $b + \tau$ signals. The background distributions (coloured histograms) are stacked and the signal distributions in both panels correspond to the LQ parameter choices $g_U = 3$, $\beta_L^{33} = 1$, $\beta_L^{23} = \beta_R^{33} = 0$ and $M_U = 1\,\text{TeV}$ (black dotted lines) or $M_U = 2\,\text{TeV}$ (black solid lines). The shown predictions are obtained assuming LHC collisions at a CM energy of 14 TeV.

for them. While for LQ realisations (3.1) with $\beta_L^{23} = 0$ only the strategy targeting the $2 \to 2$ process is relevant, in all other cases both analyses can be applied. Furthermore, in the event that a LQ signal is observed, the relative rate in the two signal regions can be used to determine the composition of the signal which itself is controlled by the couplings β_L^{33}, β_L^{23} and β_R^{33}.

In the case of the $2 \to 2$ process the entire amount of E_T^{miss} stems from the neutrino produced in the decay of the τ. It follows that the transverse mass m_T^τ built from τ_{had} and E_T^{miss} has an edge at the tau mass, which in practice is smeared by the experimental resolution on τ_{had} and E_T^{miss}. In fact, the experimental distribution of m_T^τ displays a significant high-energy tail as well, corresponding to events where a semileptonic B-meson decay occurs inside the b-jet. In order to allow for a clean kinematic reconstruction of the b-τ_{had}-ν_τ system we require the azimuthal angle $\Delta\phi_{\tau\nu}$ between τ_{had} and $\vec{p}_T^{\,\text{miss}}$ to be smaller than 0.4, and $m_T^\tau < 40\,\text{GeV}$, which efficiently select
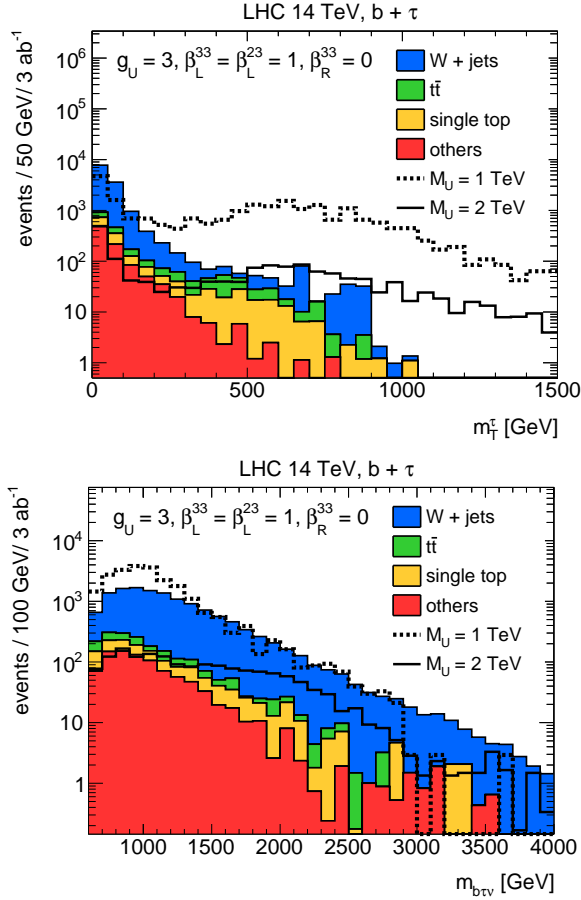
Figure 3. As Figure 2 but for the LQ coupling choices $g_U = 3, \beta_L^{33} = \beta_L^{23} = 1, \beta_R^{33} = 0$.

events that contain only the tau neutrino from the hadronic decay of the τ. Notice that the cut on m_T^τ in addition rejects SM events where a τ and a neutrino arise from a W-boson decay. This feature is illustrated in the upper panel of Figure 2 which shows the m_T^τ distribution for the background and two LQ parameter choices. The displayed distributions are obtained after application of the selection criteria given above plus the requirement $p_T(\tau_{\mathrm{had}}) > 300\,\mathrm{GeV}$. An additional variable useful for the discrimination of signal and background is the ratio $E_T^{\mathrm{miss}}/p_T(\tau_{\mathrm{had}})$. For the $2 \to 2$ process all of the E_T^{miss} comes from the neutrinos from the τ decay, and therefore $p_T(\tau_{\mathrm{had}})$ will be shared by the decay products depending on the mass and the orientation of the final-state particles. The backgrounds are dominated by events where the τ is accompanied by an additional neutrino, which implies that the ratio $E_T^{\mathrm{miss}}/p_T(\tau_{\mathrm{had}})$ is typically higher for the signal than for the background.

For signal events where an on-shell LQ is produced, the τ from the LQ decay will be highly boosted, and as a result the momentum of the neutrino will tend to be aligned with the momentum of the τ_{had}. In this situation the invariant mass $m_{b\tau\nu}$ of the b-jet and the τ can be fully reconstructed, and $m_{b\tau\nu}$ is predicted to peak at the LQ mass. In the lower panel of Figure 2 we show the $m_{b\tau\nu}$ distribution for two LQ masses and the parameter choice $\beta_L^{33} = 1, \beta_L^{23} = \beta_R^{33} = 0$, after imposing the cut $p_T(\tau_{\mathrm{had}}) > 300\,\mathrm{GeV}$ in addition to the selections described above. One observes that the
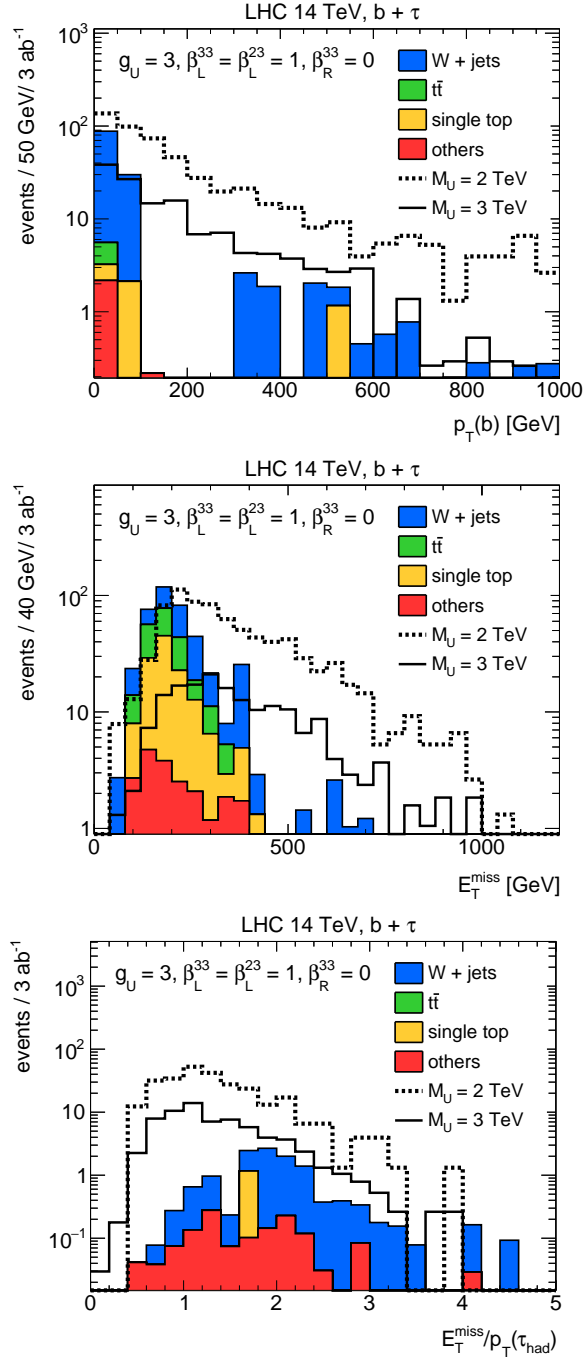
Figure 4. $p_T(b)$ (upper panel), E_T^{miss} (middle panel) and $E_T^{\mathrm{miss}}/p_T(\tau_{\mathrm{had}})$ (lower panel) distribution for the background and two $b + \tau$ signals after the selections for the $2 \to 3$ process as described in the main text. The displayed signal distributions correspond to $M_U = 2\,\mathrm{TeV}$ (black dotted lines) and $M_U = 3\,\mathrm{TeV}$ (black solid lines), while the other LQ parameters are the same as those used to obtain Figure 3.

requirement $|m_{b\tau\nu} - M_U| < 200\,\mathrm{GeV}$ with M_U denoting the nominal LQ mass efficiently selects the resonant decay of the LQ. One also sees from this figure that the background is a steeply falling

distribution which is dominated by W + jets production. The final selection in the case of the $2 \rightarrow 2$ process is obtained by imposing the latter requirement, by requiring $E_T^{\text{miss}}/p_T(\tau_{\text{had}}) < 0.3$ and by hardening the $p_T(\tau_{\text{had}})$ threshold to a value between $300\,\text{GeV}$ and $600\,\text{GeV}$ depending on the LQ mass under consideration.

For the $2 \rightarrow 3$ process the additional hard neutrino produced alongside the LQ completely changes the kinematics. The effect can be observed in Figure 3, where the distributions for the same variables as in Figure 2 are shown. The same cuts are applied except for $\Delta\phi_{\tau\nu} < 0.4$, and the shown LQ signals correspond to the parameter choices $\beta_L^{33} = \beta_L^{23} = 1, \beta_R^{33} = 0$. As displayed in the upper panel of Figure 3, in the case of the m_T^τ distribution the signal displays a peak at $m_T^\tau = 0$, corresponding to the $2 \rightarrow 2$ component, and a broad enhancement for $m_T^\tau > 300\,\text{GeV}$. The background is dominated by processes including the decay of a single W boson, for which m_T^τ is bounded at the parton level from above by the W-boson mass. A lower limit on m_T^τ of a few hundred GeV is therefore useful to reduce the backgrounds. Notice that as a result of the different m_T^τ selection and the missing $\Delta\phi_{\tau\nu}$ cut, the peak in the $m_{b\tau\nu}$ distribution corresponding to the $2 \rightarrow 2$ process is largely washed out in signal samples that receive contributions from both $b\tau \rightarrow U \rightarrow b\tau$ and $gc \rightarrow U\nu_\tau \rightarrow b\tau\nu_\tau$ scattering. See the lower panel in Figure 3 for an example distribution.

The selection $m_{b\tau} > 160\,\text{GeV}$ imposed on the invariant mass of the b and the τ_{had} further suppresses the SM background including events results stemming from top-quark decays. An additional background rejection is achieved by requiring $p_T(b) > 100\,\text{GeV}$, $p_T(\tau_{\text{had}}) > 200\,\text{GeV}$, $E_T^{\text{miss}} > 400\,\text{GeV}$ and $E_T^{\text{miss}}/p_T(\tau_{\text{had}}) < 1.5$. The $p_T(b)$, the E_T^{miss} and the $E_T^{\text{miss}}/p_T(\tau_{\text{had}})$ distributions after all cuts, besides the cut on the displayed variable, plus the requirement $m_T^\tau > 400\,\text{GeV}$ are displayed in Figure 4. In the case of the first two distributions one sees that the signal spectra fall off significantly slower than the corresponding background distributions. For the observable $E_T^{\text{miss}}/p_T(\tau_{\text{had}})$ the background is instead suppressed for low values of the ratio. The final selection is achieved by requiring and with a variable lower limit on m_T^τ in the range between $400\,\text{GeV}$ and $600\,\text{GeV}$.

5.2 Mono-top final state

The mono-top signature featuring the production of a top quark recoiling against an invisible particle has been studied at the LHC [84, 85] in the framework of dark matter (DM) searches. Two types of top-quark decays can be used to analyse this signature, namely the semi-leptonic and the fully hadronic decay. Notice that for boosted top quarks such as those produced in the decay of a heavy LQ targeting the fully hadronic final state requires the reconstruction of hadronic decays of the W boson through jet substructure techniques. In order to avoid this complication, we concentrate in our work on the final state that arises from semi-leptonic top decays which is easier to simulate with a simple parametrised technique. The final state of interest thus includes an isolated lepton (e or μ) a b-tagged jet and E_T^{miss} associated to two (three) neutrinos for the $2 \rightarrow 2$ ($2 \rightarrow 3$) process. Although they lead to a somewhat different final-state kinematics the $2 \rightarrow 2$ and $2 \rightarrow 3$ mono-top processes cannot be cleanly separated as in the case of the $b + \tau$ final state. We therefore develop an analysis strategy valid for both cases and provide results with the two different topologies combined.

The basic selections in our mono-top analysis are one lepton with $p_T(\ell) > 30\,\text{GeV}$ and one b-jet with $p_T(b) > 50\,\text{GeV}$ both within $|\eta| < 2.5$. Additional leptons and b-jets are vetoed, and any
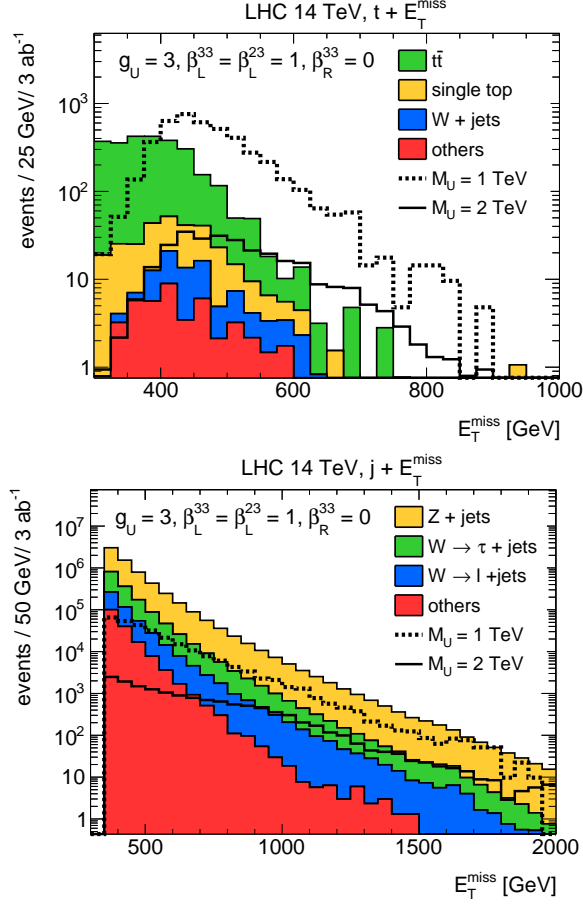
Figure 5. Upper panel: E_T^{miss} distribution for the background and two $t+E_T^{\text{miss}}$ signals. Lower panel: E_T^{miss} distribution for the background and two $j + E_T^{\text{miss}}$ signals. The background distributions (coloured histograms) are stacked and the signal distributions in both panels correspond to $g_U = 3$, $\beta_L^{33} = \beta_L^{23} = 1$, $\beta_R^{33} = 0$ and $M_U = 1$ TeV (black dotted lines) or $M_U = 2$ TeV (black solid lines). The displayed predictions are obtained for LHC collisions at 14 TeV.

additional light-flavour jet in the event is required to have $p_T(j) < 50$ GeV. The main handle to reject the SM background is the transverse mass m_T^ℓ built from the lepton momentum and E_T^{miss}. The requirement $m_T^\ell > 250$ GeV suppresses all backgrounds with a single neutrino that result from a W-boson decay. The requirement $m_{b\ell} < 140$ GeV with $m_{b\ell}$ the invariant mass of the lepton and the b-jet ensures in addition that the two particles are compatible with the decay of a top quark. In order to guarantee that the top quark is boosted, the sum of the transverse momenta of the lepton and the b-jet is required to satisfy $p_T(\ell) + p_T(b) > 400$ GeV, and the angular distance between them to be $\Delta R_{\ell b} = \sqrt{\Delta\eta_{\ell b}^2 + \Delta\phi_{\ell b}^2} < 1$. Here $\Delta\phi_{\ell b}$ denotes the difference in azimuthal angle between the lepton and the b-jet. The final selection consists in setting a lower limit on the value of E_T^{miss} dependent on precise value of the LQ mass. The upper panel of Figure 5 shows the E_T^{miss} distribution for the background and two mono-top signals after imposing all the discussed cuts.

5.3 Mono-jet final state

In the mono-jet case the relevant LQ signature consists of one high-transverse momentum c-jet and E_T^{miss} associated to either one or two neutrinos in the case of the $2 \to 2$ or the $2 \to 3$ topology. Although c-jets can be experimentally tagged at the LHC — for actual ATLAS and CMS analyses relying on c-tagging see [86–88] — a high-transverse momentum mono-charm analysis has not been performed by the LHC experiments. We therefore do not attempt to exploit the fact that the jet in the LQ mono-jet signature results from a c quark, but perform a flavour-blind $j + E_T^{\text{miss}}$ analysis to target the $c\bar{\nu}_\tau(\nu_\tau)$ final state. Our analysis hence resembles the canonical approach of searching for DM at the LHC, which has received much experimental [77, 89–91] and theoretical [92] attention, resulting in high-precision estimates of the dominant E_T^{miss} backgrounds associated to the production of a Z or W boson accompanied by at least one high-transverse momentum jet.

We use as a reference the ATLAS analysis described in [77] but employ a higher E_T^{miss} cut of $E_T^{\text{miss}} > 350\,\text{GeV}$, which reflects the fact that we are aiming for the energetic decay products of a LQ with a mass in excess of 1 TeV. We require the presence of a high-transverse momentum jet with $p_T(j) > 150\,\text{GeV}$ within $|\eta| < 2.4$, and no more than four jets with $p_T(j) > 30\,\text{GeV}$ within $|\eta| < 2.8$. The selection $\Delta\phi_{\text{min}} > 0.4$, where $\Delta\phi_{\text{min}}$ is the minimum angular difference in the azimuthal plane between a reconstructed jet and E_T^{miss}, is used to fully suppress the multi-jet background. All events containing a reconstructed electron or muon, or the hadronic decay of a τ are rejected. The sensitivity of the search is extracted through a multi-bin comparison of the shapes of the E_T^{miss} variable for the LQ signal and the LQ signal plus the SM background. Our shape fit covers eight bins between 350 GeV and 2 TeV with an additional overflow bin for events with $E_T^{\text{miss}} > 2\,\text{TeV}$. E_T^{miss} distributions for the background and two mono-jet signals after applying the discussed selections are displayed in the lower panel of Figure 5.

6 Numerical results

On the basis of the selection criteria defined in Section 5, we will study the LHC sensitivity to the three LQ signatures discussed previously assuming integrated luminosities of $300\,\text{fb}^{-1}$ and $3\,\text{ab}^{-1}$. These luminosities correspond to the full statistics expected after LHC Run III and the HL-LHC phase, respectively. For each signature and each point in the LQ parameter space we evaluate the value of the cross section which can be excluded at 95% confidence level (CL) normalised to the nominal LO cross section for the relevant model realisation as calculated by `MadGraph5_aMCNLO`. The experimental sensitivity is evaluated using a test statistics based on a profiled likelihood ratio and we make use of the CLs method [93] as implemented in the `RooStat` toolkit [94].

In the case of the $b + \tau$ and the mono-top signature, we assume systematic uncertainties of 15% and 5% on the SM backgrounds and on the signal, respectively. As explained above, in our mono-jet analysis we adopt a selection which closely resembles the signal region IM3 of the latest ATLAS $j + E_T^{\text{miss}}$ search which is based on $139\,\text{fb}^{-1}$ of LHC Run II data [77]. The systematic uncertainty quoted by ATLAS in this signal region is 1.4%, and we adopt this value as the systematic uncertainty on the total number of background events. Since we perform a fit to the shape of the E_T^{miss} distribution, we also need to take into account uncertainties related to the E_T^{miss} shape. For each of the E_T^{miss} bins considered in the analysis, ATLAS provides an uncertainty which increases from approximately 1.4% to 4% between 350 GeV to 1.2 TeV. We apply these systematic uncertainties as
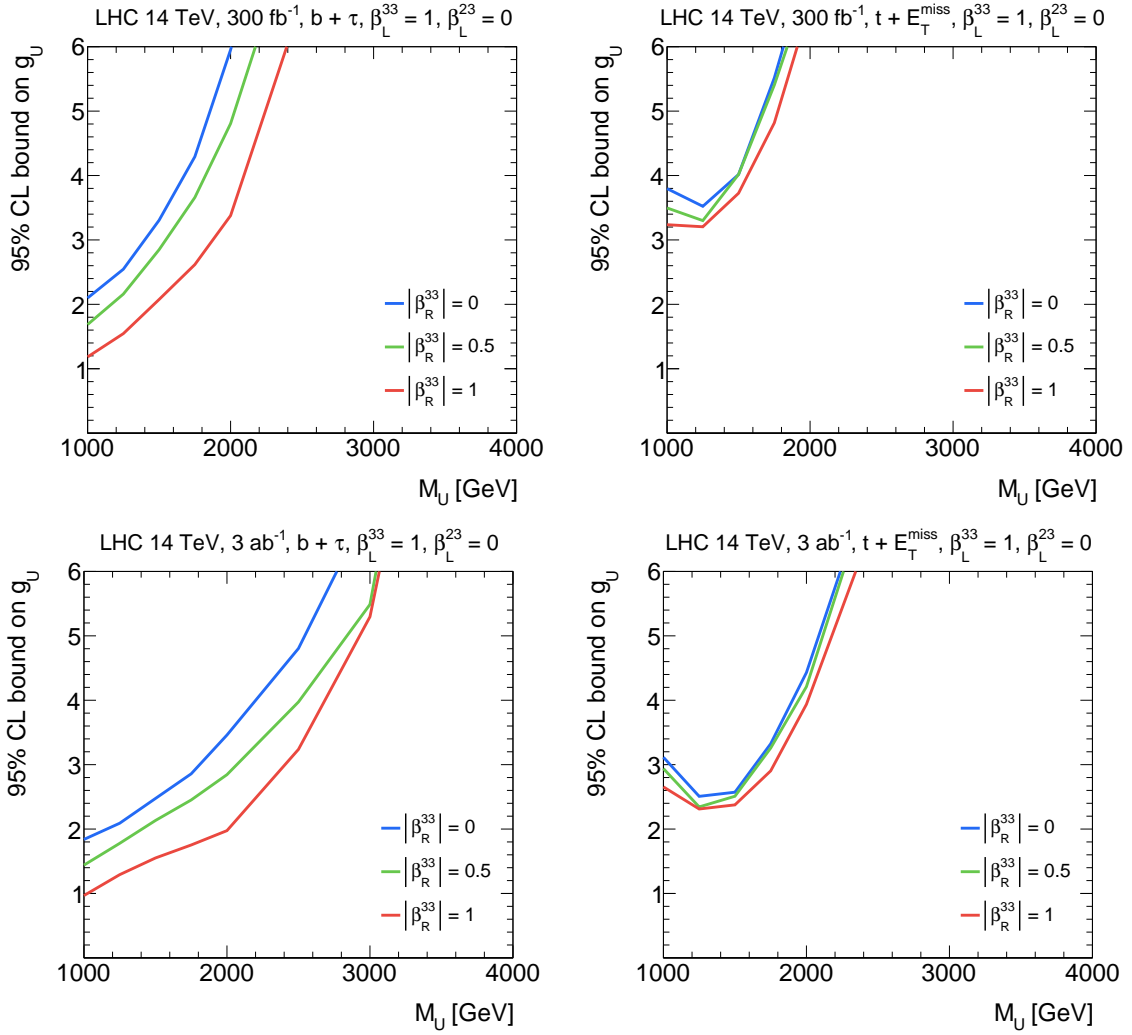
Figure 6. 95% CL exclusions in the $M_U - g_U$ plane following from the $b + \tau$ search (left) and the $t + E_T^{\text{miss}}$ search (right). The shown constraints employ the LQ parameters $\beta_L^{33} = 1$, $\beta_L^{23} = 0$ and $\left|\beta_R^{33}\right| = \{0, 0.5, 1\}$, and parameter regions above and to the left of the coloured lines are excluded. The upper (lower) panels assume $300\,\text{fb}^{-1}$ ($3\,\text{ab}^{-1}$) of LHC collisions at $14\,\text{TeV}$.

bin-by-bin shape uncertainties in our fit. For the bins between $1.5\,\text{TeV}$ and $2\,\text{TeV}$ we furthermore assume an uncertainty of 5%, while we take an uncertainty of 8% for the total number of events with $E_T^{\text{miss}} > 2\,\text{TeV}$. Notice that our uncertainty treatment corresponds to taking the uncertainties among different E_T^{miss} bins to be uncorrelated. In addition, since the statistical uncertainties of the control regions that are used to constrain the background will get reduced with more luminosity, also the systematic uncertainties are expected to decrease with larger data samples. We therefore believe that our mono-jet study provides conservative results when applied to the full LHC Run III and HL-LHC data sets.
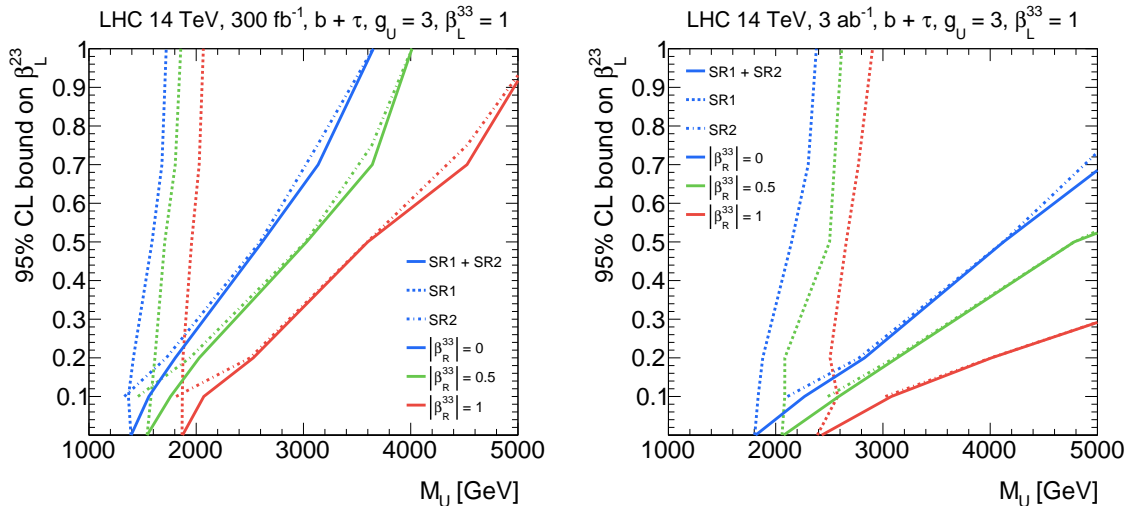
Figure 7. 95% CL exclusion following from the $b + \tau$ search in the $M_U\text{–}\beta_L^{23}$ plane assuming $300 \, \text{fb}^{-1}$ (left) and $3 \, \text{ab}^{-1}$ (right) of LHC 14 TeV data. The parameter regions above and to the left of the coloured lines are excluded. The shown constraints are obtained for $g_U = 3$, $\beta_L^{33} = 1$ and $\left|\beta_R^{33}\right| = \{0, 0.5, 1\}$. The dotted, dash-dotted and solid lines illustrate the bounds arising from signal region one (SR1), signal region two (SR2) and their combination (SR1 + SR2), respectively.

In order to allow for an easy comparison with the comprehensive analysis [53] of LHC constraints on the singlet vector LQ model, we adopt the choice $\beta_L^{33} = 1$, permit variations of β_L^{23} and consider the following three benchmarks $\left|\beta_R^{33}\right| = \{0, 0.5, 1\}$ for the right-handed coupling β_R^{33}. We begin our numerical study by considering LQ realisations (2.1) with $\beta_L^{23} = 0$. In this case the dominant constraints on the parameter space (3.1) arise from the proposed $b + \tau$ and mono-top searches. The 95% CL exclusion limits in the $M_U\text{–}g_U$ plane that are obtained from the analyses described in Sections 5.1 and 5.2 are shown in the panels of Figure 6. To obtain the displayed results we have set $\beta_L^{33} = 1$. From the panels it is evident that the $b + \tau$ search generically leads to stronger constraints on g_U than the mono-top search. Furthermore, the limits from the $b + \tau$ search become notably stronger for non-zero β_R^{33}, because both the $b\tau \to U$ production cross section and the $U \to b\tau$ branching ratio are enhanced by $\left|\beta_R^{33}\right|^2$. In the mono-top case, the relevant $U \to t\nu_\tau$ branching ratio is instead proportional to $1/\left|\beta_R^{33}\right|^2$ and as a result the derived constraints are to first approximation independent of β_R^{33}. We furthermore observe that for $M_U = 1 \, \text{TeV}$ ($M_U = 3 \, \text{TeV}$) the 95% CL limits on g_U that can be set at the HL-LHC is by a factor of around 1.5 (3.8) better than the bound that LHC Run III is expected to place. This statement applies to both search strategies considered in the panels of Figure 6. Notice finally that for the largest values of g_U shown in the latter figure, i.e. $g_U \simeq 6$, higher-order radiative corrections are expected to become numerically important, and as a result the derived limits are less reliable in this region.

So far we have in this section only studied LQ realisations with no second-third-generation left-handed mixing, i.e. $\beta_L^{23} = 0$. We now allow for $\beta_L^{23} \neq 0$ in which case one has to take into account the contributions from both the $2 \to 2$ and the $2 \to 3$ process (see Figure 1). In Figure 7 we show the 95% CL exclusion n the $M_U\text{–}\beta_L^{23}$ plane that derive from our $b + \tau$ search strategies. The
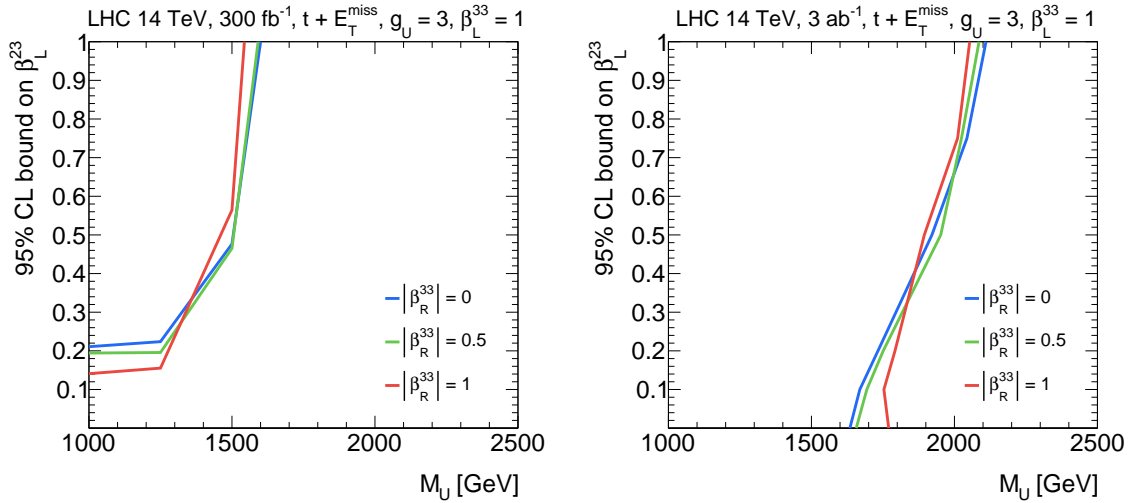
Figure 8. As Figure 7 but for the $t + E_T^{\mathrm{miss}}$ search. The shown exclusions correspond to the mono-top search including both the $2 \to 2$ and the $2 \to 3$ process.

corresponding parameter choices are $g_U = 3$, $\beta_L^{33} = 1$ and $\left|\beta_R^{33}\right| = \{0, 0.5, 1\}$. The bounds arising from signal region one (SR1), signal region two (SR2) and their combination (SR1 + SR2) are indicated as dotted, dash-dotted and solid lines, respectively — cf. Section 5.1 for the precise definition of the signal regions. SR1 targets the $2 \to 2$ process and one observes that the corresponding limits are largely independent from β_L^{23}. This behaviour can be understood by noticing that for $\beta_L^{23} \neq 0$ the LQ production cross section receives contributions proportional to $\left|\beta_L^{23}\right|^2$ and $\left|\beta_L^{13}\right|^2 \simeq \lambda^2 \left|\beta_L^{23}\right|^2 \simeq 0.05 \left|\beta_L^{23}\right|^2$ from the partonic quark-lepton channels $s\tau \to U$ and $d\tau \to U$, respectively. While the $d\tau \to U$ contribution is enhanced by the down-quark PDF it is also strongly CKM suppressed, and as a result the corresponding number of signal events in SR1 amounts to no more than 10% of the total rate. It furthermore turns out that $b\tau \to U$ production provides the leading contribution to the number of events in SR1 for $\beta_L^{23} \lesssim 0.5$, while for $\beta_L^{23} \gtrsim 0.5$ the $s\tau \to U$ channel dominates. For sufficiently large β_L^{23} the LQ production cross section is thus enhanced by $\left|\beta_L^{23}\right|^2$ but since the $U \to b\tau$ branching ratio is proportional to $1/\left|\beta_L^{23}\right|^2$ the limits on M_U become almost independent of β_L^{23}.

Concerning the exclusions resulting from SR2, we first remark that the gluon-quark fusion channel $gc \to b\tau\nu_\tau$ ($gu \to b\tau\nu_\tau$) contributes around 85% (15%) of the number of events in this signal region. In fact, the largest contribution to the fiducial $gc \to b\tau\nu_\tau$ cross section arises from t-channel exchange of a U, which turns out to scale approximately as β_L^{23} after cuts. This finding explains why the constraints in the M_U–β_L^{23} plane that follow from the $b + \tau$ search in SR2 are roughly linear in β_L^{23}. Notice that the above arguments hold for any value of the third-generation right-handed quark-lepton-LQ coupling, and in consequence the shape of the $b+\tau$ exclusions in Figure 7 do not change under variations of β_R^{33} but they simply become stronger with increasing $\left|\beta_R^{33}\right|$. It is also evident from this figure that the SR2 search strategy is significantly more powerful in constraining the M_U–β_L^{23} parameter space than the SR1 search strategy. It has to be stressed, how-
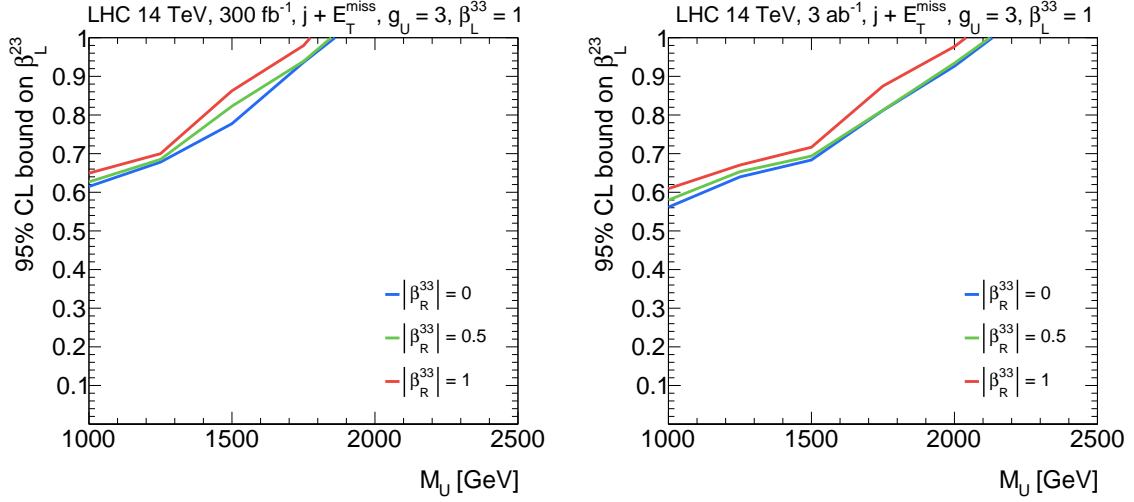
Figure 9. As Figure 8 but for the $j + E_T^{\text{miss}}$ search. Both the $2 \to 2$ and the $2 \to 3$ process are included to obtain the displayed mono-jet exclusions.

ever, that the $b + \tau$ final state resulting from the $2 \to 2$ process still plays a unique role, because in the case of a discovery, only this signature would potentially allow to determine the LQ mass by observing a peak in the $m_{b\tau\nu_\tau}$ distribution at the nominal LQ mass M_U.

In Figure 8 we display the 95% CL exclusions in the M_U–β_L^{23} plane that derive from the mono-top search strategy described in Section 5.2. The shown results correspond to the parameter choices $g_U = 3$, $\beta_L^{33} = 1$ and $\left| \beta_R^{33} \right| = \{0, 0.5, 1\}$. Like in the case of the panels on the right-hand side of Figure 6, we see that the derived constraints are to first approximation independent of the choice of β_R^{33}, because this dependence tends to cancel in the product of the production cross section and the branching ratio. One also observes that for the employed parameters it will not be possible to test models with $\beta_L^{23} = 0$ at LHC Run III for any LQ mass in the studied range. This is expected to change with higher integrated luminosities, and the HL-LHC mono-top searches should be able to ultimately exclude models with $\beta_L^{23} = 0$ up to LQ masses of $M_U \simeq 1.7 \, \text{TeV}$. Concerning the LHC Run III (HL-LHC) bounds, we mention that in the LQ parameter space close to the exclusions around 60% to 80% (70% to 100%) of the mono-top signal arises from the $2 \to 2$ process. We furthermore observe that for $\beta_L^{23} \lesssim 0.5$ the dominant mono-top production mechanism is $b\tau \to U \to t\nu_\tau$, while for $\beta_L^{23} \gtrsim 0.5$ the $s\tau \to U \to t\nu_\tau$ channel provides the leading contribution. The channel $d\tau \to U \to t\nu_\tau$ is always subleading, amounting to no more than 15% of the total $2 \to 2$ rate. In the case of the $2 \to 3$ process, we find instead that around 85% of the events arise from $gc \to U\nu_\tau \to t\nu_\tau\bar{\nu}_\tau$, while 15% are due to $gu \to U\nu_\tau \to t\nu_\tau\bar{\nu}_\tau$.

The 95% CL exclusions in the M_U–β_L^{23} plane that arise from the mono-jet analysis described in Section 5.3 can finally be seen in Figure 9. To allow for a straightforward comparison with the $b + \tau$ and mono-top limits discussed before, we have again chosen $g_U = 3$, $\beta_L^{33} = 1$ and $\left| \beta_R^{33} \right| = \{0, 0.5, 1\}$. Since the dependence on the third-generation right-handed coupling tends to cancel in the product of the production cross section and the branching ratio the obtained mono-jet limits are again largely insensitive to the choice of β_R^{33}. One also observes that compared to the

$b + \tau$ and the mono-top search, the reach of the mono-jet search is significantly weaker. In the considered LQ scenario it should be possible to exclude values $\beta_L^{23} \gtrsim 0.6$ for $M_U = 1\,\text{TeV}$, while for $\beta_L^{23} = 1$ the LHC seems to have a mass reach of $M_U \lesssim 2\,\text{TeV}$. Also notice that the shown HL-LHC exclusions are only slightly stronger than the limits obtained at LHC Run III. This is a result of the conservative treatment of systematic uncertainties in our mono-jet study.

7 Conclusions and outlook

The main goal of this article was to give additional well-motivated examples of lepton-initiated processes that can provide valuable probes of beyond the SM physics at hadron colliders once the lepton PDFs are precisely known [59]. In contrast to the recent detailed study [60] which considered minimal scalar LQs coupling to first- and second-generation leptons and quarks, we have analysed the LHC reach of resonant production modes involving third-generation singlet vector LQs. Such particles are enjoying a renaissance because they can simultaneously explain the deviations from τ-μ (and τ-e) universality seen in $b \to c\ell\nu$ transitions and the deviations from μ-e universality observed in $b \to s\ell^+\ell^-$ transitions.

We have argued that the observed B anomalies if interpreted in the context of a third-generation singlet vector LQ model strongly motivate searches for resonant LQ production in the $b + \tau$, the mono-top and the mono-jet final state. While the latter two final states have been targeted at the LHC (see for instance [77, 84, 85, 95]), searches for final states with a single bottom quark and a single tau lepton have up till now not been performed by either ATLAS nor CMS. In the case of the $b + \tau$ final state, we have designed two different analyses strategies that aim at separating the $2 \to 2$ from the $2 \to 3$ process (cf. Figure 1) by exploiting the fact that the resulting final states have very different kinematic features. Although they lead to a somewhat different final-state kinematics, in the mono-top and the mono-jet case the $2 \to 2$ and $2 \to 3$ processes cannot be cleanly separated. We have therefore developed analysis strategies valid for both cases and provide mono-top and mono-jet results with the two different topologies combined.

We have then analysed the coverage of the parameter space of the third-generation singlet vector LQ model at LHC Run III and the HL-LHC. In a first step, we have studied model realisations with no second-third-generation left-handed mixing, i.e. $\beta_L^{23} = 0$, considering the three benchmarks $\left| \beta_R^{33} \right| = \{0, 0.5, 1\}$ for the third-generation right-handed coupling. In this case the dominant 95% CL constraints in the $M_U - g_U$ plane arise from the $b + \tau$ and the mono-top search. In a second step, we have then allowed for $\beta_L^{23} \neq 0$ fixing the remaining parameters to $g_U = 3$ and $\beta_L^{33} = 1$. The two panels in Figure 10 illustrate the HL-LHC coverage of the proposed $b + \tau$, mono-top and mono-jet search strategies in the $M_U - \beta_L^{23}$ plane for $\beta_R^{33} = 0$ (left) and $\beta_R^{33} = -1$ (right). For comparison the 95% CL regions preferred by a fit to the LFU violating ratios $R_{D^{(*)}}$ (see e.g. [31, 32, 53] for details), the $pp \to \tau^+\tau^-$ limits obtained in [53] and the bounds from the recent CMS search [43] for $pp \to UU$ and $pp \to U\tau$ production are also shown as yellow contours, solid black curves and dotted black lines, respectively. Concerning the latter bound of $M_U \simeq 1.4\,\text{TeV}$, we stress that it has been obtained under the assumption that the vector LQ decays with equal branching ratios of 50% to both $b\tau^+$ and $t\bar{\nu}_\tau$ final states. Since this assumption does not hold in the entire parameter space considered in the panels of Figure 10 the shown $UU + U\tau$ exclusions have only an indicative character. From the plots in the latter figure it is evident that future LHC searches for a $b + \tau$ sig-
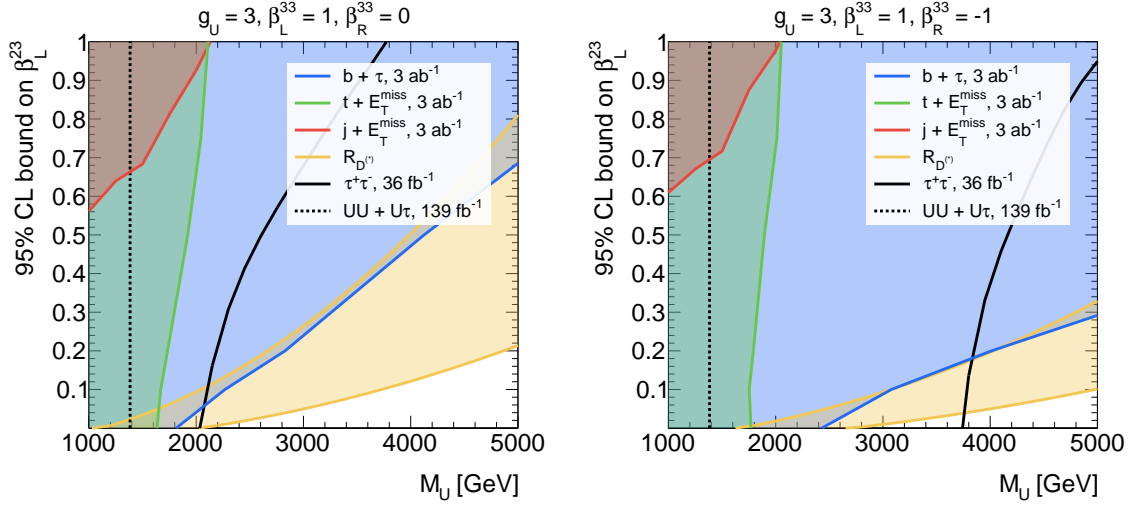
Figure 10. Current and future constraints on the third-generation singlet vector LQ in the $M_U - \beta_L^{23}$ plane. The left (right) panel corresponds to the parameter choices $g_U = 3$, $\beta_L^{33} = 1$ and $\beta_R^{33} = 0$ ($\beta_R^{33} = -1$). The shown blue, green and red regions indicated the 95% CL exclusions that derive from the proposed $b + \tau$, $t + E_T^{miss}$ and $j + E_T^{miss}$ search strategies assuming $3\,\mathrm{ab}^{-1}$ of LHC 14 TeV data. For comparison also the regions favoured by the $b \to c\ell\nu$ data ($R_{D^{(*)}}$), the bounds that have been derived in [53] from di-tau ($\tau^+\tau^-$) production and the limits following from the recent CMS search for pair and single third-generation LQ signatures ($UU + U\tau$) [43] are indicated as yellow contours, solid black curves and dotted black lines, respectively. The displayed $\tau^+\tau^-$ ($UU + U\tau$) constraints correspond to $36\,\mathrm{fb}^{-1}$ ($139\,\mathrm{fb}^{-1}$) of LHC 13 TeV data. See text for further details.

nature will allow to exclude a relevant portion of the parameter space preferred by the *B*-physics anomalies in several models with third-generation singlet vector LQs. In order to further illustrate the latter statement, we show in Figure 11 the HL-LHC coverage of our $b + \tau$ search strategy in the $M_U - g_U$ plane for $\beta_L^{33} = 1$ and $\beta_L^{23} = 0.2$. This is a representative benchmark to simultaneously address both the $R_{D^{(*)}}$ and the $R_{K^{(*)}}$ anomalies. The left and right panel corresponds to $\beta_R^{33} = 0$ and $\beta_R^{33} = -1$, respectively. For comparison the 95% CL constraints following from the proposed mono-top search strategy (green contours), $R_{D^{(*)}}$ (yellow contours), $pp \to \tau^+\tau^-$ (solid black lines) and $pp \to UU + U\tau$ production (dotted black lines) are shown as well. One observes that for $\beta_R^{33} = 0$ ($\beta_R^{33} = -1$), HL-LHC searches for $b\tau$ final states should allow to test third-generation singlet vector LQ explanations of the *B*-physics anomalies for LQ masses up to around 3 TeV (4 TeV). We thus encourage the ATLAS and the CMS collaboration to perform dedicated resonance searches in final states featuring a single bottom quark and a single tau lepton, a signature that has so far not been explored by them.

The results presented in this article also call for further theoretical developments concerning the accurate predictions of LHC processes that are induced by quark-lepton annihilation. While the lepton PDFs are now accurately known, official PS codes can at present not correctly handle incoming leptons. In addition, fully differential NLO QCD and QED hadron-collider predictions are not available for processes like $b\tau \to U \to b\tau$ — a first step into this direction has been made very recently in [61] by calculating the NLO QCD and QED corrections to the inclusive quark-lepton
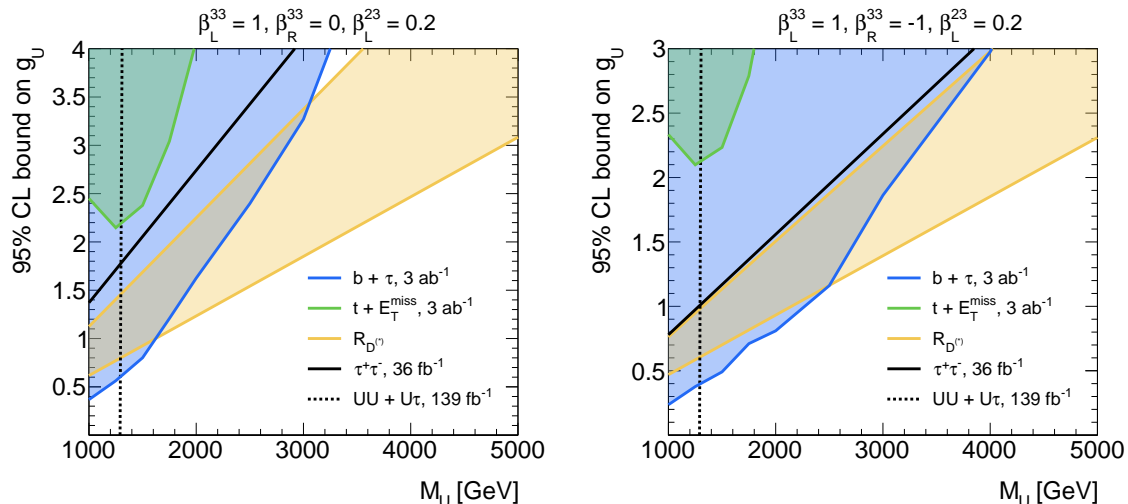
Figure 11. Current and future constraints on the third-generation singlet vector LQ in the $M_U - g_U$ plane. The left (right) panel corresponds to the benchmarks $\beta_L^{33} = 1$, $\beta_R^{33} = 0$ ($\beta_R^{33} = -1$) and $\beta_L^{23} = 0.2$. The colour and style coding of the shown constraints are the same as those displayed in Figure 10. Since for $\beta_L^{23} = 0.2$, the proposed $j + E_T^{\text{miss}}$ search strategy does lead to bounds $g_U > 4$ even at the HL-LHC with $3\,\text{ab}^{-1}$ of integrated luminosity, mono-jet constraints do not appear in the two panels.

induced cross sections of singly-produced scalar LQs. Once fully differential NLO QCD and QED corrections are available, they should be consistently combined with the PS to obtain NLO+PS predictions that provide an accurate modelling of the exclusive final states targeted at the LHC by ATLAS and CMS.

Acknowledgments

References

[1] J. Lees *et al.* (BaBar), Phys. Rev. Lett. **109**, 101802 (2012), arXiv:1205.5442 [hep-ex].

[2] M. Huschle *et al.* (Belle), Phys. Rev. D **92**, 072014 (2015), arXiv:1507.03233 [hep-ex].

[3] R. Aaij *et al.* (LHCb), Phys. Rev. Lett. **115**, 111803 (2015), [Erratum: Phys. Rev. Lett. 115, 159901 (2015)], arXiv:1506.08614 [hep-ex].

[4] Y. Sato *et al.* (Belle), Phys. Rev. D **94**, 072007 (2016), arXiv:1607.07923 [hep-ex].

[5] S. Hirose *et al.* (Belle), Phys. Rev. Lett. **118**, 211801 (2017), arXiv:1612.00529 [hep-ex].

[6] R. Aaij *et al.* (LHCb), Phys. Rev. Lett. **120**, 171802 (2018), arXiv:1708.08856 [hep-ex].

[7] R. Aaij *et al.* (LHCb), Phys. Rev. Lett. **113**, 151601 (2014), arXiv:1406.6482 [hep-ex].

[8] R. Aaij *et al.* (LHCb), JHEP **08**, 055 (2017), arXiv:1705.05802 [hep-ex].

[9]   R. Alonso, B. Grinstein, and J. Martin Camalich, JHEP **10**, 184 (2015), arXiv:1505.05164 [hep-ph].

[10] L. Calibbi, A. Crivellin, and T. Ota, Phys. Rev. Lett. **115**, 181801 (2015), arXiv:1506.02661 [hep-ph].

[11] S. Fajfer and N. Košnik, Phys. Lett. B **755**, 270 (2016), arXiv:1511.06024 [hep-ph].

[12] R. Barbieri, G. Isidori, A. Pattori, and F. Senia, Eur. Phys. J. C **76**, 67 (2016), arXiv:1512.01560 [hep-ph].

[13] G. Hiller, D. Loose, and K. Schönwald, JHEP **12**, 027 (2016), arXiv:1609.08895 [hep-ph].

[14] B. Bhattacharya, A. Datta, J.-P. Guévin, D. London, and R. Watanabe, JHEP **01**, 015 (2017), arXiv:1609.09078 [hep-ph].

[15] R. Barbieri, C. W. Murphy, and F. Senia, Eur. Phys. J. C **77**, 8 (2017), arXiv:1611.04930 [hep-ph].

[16] D. Buttazzo, A. Greljo, G. Isidori, and D. Marzocca, JHEP **11**, 044 (2017), arXiv:1706.07808 [hep-ph].

[17] N. Assad, B. Fornal, and B. Grinstein, Phys. Lett. B **777**, 324 (2018), arXiv:1708.06350 [hep-ph].

[18] L. Di Luzio, A. Greljo, and M. Nardecchia, Phys. Rev. D **96**, 115011 (2017), arXiv:1708.08450 [hep-ph].

[19] L. Calibbi, A. Crivellin, and T. Li, Phys. Rev. D **98**, 115002 (2018), arXiv:1709.00692 [hep-ph].

[20] M. Bordone, C. Cornella, J. Fuentes-Martin, and G. Isidori, Phys. Lett. B **779**, 317 (2018), arXiv:1712.01368 [hep-ph].

[21] R. Barbieri and A. Tesi, Eur. Phys. J. C **78**, 193 (2018), arXiv:1712.06844 [hep-ph].

[22] M. Blanke and A. Crivellin, Phys. Rev. Lett. **121**, 011801 (2018), arXiv:1801.07256 [hep-ph] .

[23] A. Greljo and B. A. Stefanek, Phys. Lett. B **782**, 131 (2018), arXiv:1802.04274 [hep-ph].

[24] M. Bordone, C. Cornella, J. Fuentes-Martín, and G. Isidori, JHEP **10**, 148 (2018), arXiv:1805.09328 [hep-ph].

[25] J. Kumar, D. London, and R. Watanabe, Phys. Rev. D **99**, 015007 (2019), arXiv:1806.07403 [hep-ph].

[26] A. Azatov, D. Barducci, D. Ghosh, D. Marzocca, and L. Ubaldi, JHEP **10**, 092 (2018), arXiv:1807.10745 [hep-ph].

[27] L. Di Luzio, J. Fuentes-Martin, A. Greljo, M. Nardecchia, and S. Renner, JHEP **11**, 081 (2018), arXiv:1808.00942 [hep-ph].

[28] A. Angelescu, D. Bečirević, D. Faroughy, and O. Sumensari, JHEP **10**, 183 (2018), arXiv:1808.08179 [hep-ph].

[29] M. Schmaltz and Y.-M. Zhong, JHEP **01**, 132 (2019), arXiv:1810.10017 [hep-ph].

[30] B. Fornal, S. A. Gadam, and B. Grinstein, Phys. Rev. D **99**, 055025 (2019), arXiv:1812.01603 [hep-ph].

[31] J. Aebischer, W. Altmannshofer, D. Guadagnoli, M. Reboud, P. Stangl, and D. M. Straub, Eur. Phys. J. C **80**, 252 (2020), arXiv:1903.10434 [hep-ph].

[32] C. Cornella, J. Fuentes-Martin, and G. Isidori, JHEP **07**, 168 (2019), arXiv:1903.11517 [hep-ph].

[33] R.-X. Shi, L.-S. Geng, B. Grinstein, S. Jäger, and J. Martin Camalich, JHEP **12**, 065 (2019), arXiv:1905.08498 [hep-ph].

[34] L. Da Rold and F. Lamagna, JHEP **12**, 112 (2019), arXiv:1906.11666 [hep-ph].

[35] M. Bordone, O. Català, and T. Feldmann, JHEP **01**, 067 (2020), arXiv:1910.02641 [hep-ph].

[36] A. Crivellin, D. Müller, and F. Saturnino, JHEP **06**, 020 (2020), arXiv:1912.04224 [hep-ph].

[37] W. Altmannshofer, S. Gori, H. H. Patel, S. Profumo, and D. Tuckler, JHEP **05**, 069 (2020), arXiv:2002.01400 [hep-ph].

[38] S. Iguro, M. Takeuchi, and R. Watanabe, (2020), arXiv:2011.02486 [hep-ph].

[39] A. M. Sirunyan *et al.* (CMS), Phys. Rev. Lett. **121**, 241802 (2018), arXiv:1809.05558 [hep-ex].

[40] A. M. Sirunyan *et al.* (CMS), JHEP **03**, 170 (2019), arXiv:1811.00806 [hep-ex].

[41] M. Aaboud *et al.* (ATLAS), JHEP **06**, 144 (2019), arXiv:1902.08103 [hep-ex].

[42] G. Aad *et al.* (ATLAS), (2020), arXiv:2010.02098 [hep-ex].

[43] A. M. Sirunyan *et al.* (CMS), (2020), arXiv:2012.04178 [hep-ex].

[44] T. Mandal, S. Mitra, and S. Seth, JHEP **07**, 028 (2015), arXiv:1503.04689 [hep-ph].

[45] I. Doršner, S. Fajfer, A. Greljo, J. Kamenik, and N. Košnik, Phys. Rept. **641**, 1 (2016), arXiv:1603.04993 [hep-ph].

[46] D. A. Faroughy, A. Greljo, and J. F. Kamenik, Phys. Lett. **B764**, 126 (2017), arXiv:1609.07138 [hep-ph].

[47] N. Raj, Phys. Rev. D **95**, 015011 (2017), arXiv:1610.03795 [hep-ph].

[48] I. Doršner and A. Greljo, JHEP **05**, 126 (2018), arXiv:1801.07641 [hep-ph].

[49] G. Hiller, D. Loose, and I. Nišandžić, Phys. Rev. D **97**, 075004 (2018), arXiv:1801.09399 [hep-ph] .

[50] S. Bansal, R. M. Capdevilla, A. Delgado, C. Kolda, A. Martin, and N. Raj, Phys. Rev. D **98**, 015037 (2018), arXiv:1806.02370 [hep-ph].

[51] A. Sirunyan *et al.* (CMS), JHEP **07**, 115 (2018), arXiv:1806.03472 [hep-ex].

[52] T. Mandal, S. Mitra, and S. Raz, Phys. Rev. D **99**, 055028 (2019), arXiv:1811.03561 [hep-ph].

[53] M. J. Baker, J. Fuentes-Martín, G. Isidori, and M. König, Eur. Phys. J. C **79**, 334 (2019), arXiv:1901.10480 [hep-ph].

[54] K. Chandak, T. Mandal, and S. Mitra, Phys. Rev. D **100**, 075019 (2019), arXiv:1907.11194 [hep-ph].

[55] C. Borschensky, B. Fuks, A. Kulesza, and D. Schwartländer, Phys. Rev. D **101**, 115017 (2020), arXiv:2002.08971 [hep-ph].

[56] D. Buttazzo, D. Marzocca, M. Nardecchia, P. Pani, and G. Polesello, *LHC sensitivity to leptoquark production in τ + heavy quark final states* in G. Brooijmans *et al., 11th Les Houches Workshop on Physics at TeV Colliders: PhysTeV Les Houches* (2020), arXiv:2002.12220 [hep-ph] .

[57] A. Bhaskar, T. Mandal, and S. Mitra, (2020), arXiv:2004.01096 [hep-ph].

[58] J. Ohnemus, S. Rudaz, T. Walsh, and P. Zerwas, Phys. Lett. B **334**, 203 (1994), arXiv:hep-ph/9406235.

[59] L. Buonocore, P. Nason, F. Tramontano, and G. Zanderighi, JHEP **08**, 019 (2020), arXiv:2005.06477 [hep-ph].

[60] L. Buonocore, U. Haisch, P. Nason, F. Tramontano, and G. Zanderighi, Phys. Rev. Lett. **125**, 231804 (2020), arXiv:2005.06475 [hep-ph].

[61] A. Greljo and N. Selimovic, (2020), arXiv:2012.02092 [hep-ph].

[62] V. Bertone, S. Carrazza, N. P. Hartland, and J. Rojo (NNPDF), SciPost Phys. **5**, 008 (2018), arXiv:1712.07053 [hep-ph] .

[63] J. Alwall, R. Frederix, S. Frixione, V. Hirschi, F. Maltoni, O. Mattelaer, H. S. Shao, T. Stelzer, P. Torrielli, and M. Zaro, JHEP **07**, 079 (2014), arXiv:1405.0301 [hep-ph].

[64] T. Sjöstrand, S. Ask, J. R. Christiansen, R. Corke, N. Desai, P. Ilten, S. Mrenna, S. Prestel, C. O. Rasmussen, and P. Z. Skands, Comput. Phys. Commun. **191**, 159 (2015), arXiv:1410.3012 [hep-ph].

[65] U. Haisch and G. Polesello, JHEP **02**, 029 (2019), arXiv:1812.00694 [hep-ph].

[66] J. M. Campbell, R. K. Ellis, P. Nason, and E. Re, JHEP **04**, 114 (2015), arXiv:1412.1828 [hep-ph].

[67] E. Re, Eur. Phys. J. **C71**, 1547 (2011), arXiv:1009.2450 [hep-ph].

[68] T. Melia, P. Nason, R. Röntsch, and G. Zanderighi, JHEP **11**, 078 (2011), arXiv:1107.5051 [hep-ph].

[69] P. Nason and G. Zanderighi, Eur. Phys. J. **C74**, 2702 (2014), arXiv:1311.1365 [hep-ph].

[70] S. Alioli, P. Nason, C. Oleari, and E. Re, JHEP **1006**, 043 (2010), arXiv:1002.2581 [hep-ph].

[71] M. Czakon and A. Mitov, Comput. Phys. Commun. **185**, 2930 (2014), arXiv:1112.5675 [hep-ph].

[72] M. Czakon, P. Fiedler, and A. Mitov, Phys. Rev. Lett. **110**, 252004 (2013), arXiv:1303.6254 [hep-ph].

[73] C. Anastasiou, L. J. Dixon, K. Melnikov, and F. Petriello, Phys. Rev. **D69**, 094008 (2004), arXiv:hep-ph/0312266 [hep-ph] .

[74] R. Gavin, Y. Li, F. Petriello, and S. Quackenbush, Comput. Phys. Commun. **184**, 208 (2013), arXiv:1201.5896 [hep-ph].

[75] U. Haisch and G. Polesello, JHEP **02**, 128 (2019), arXiv:1812.08129 [hep-ph].

[76] S. Catani, F. Krauss, R. Kuhn, and B. R. Webber, JHEP **11**, 063 (2001), arXiv:hep-ph/0109231 [hep-ph].

[77] *Search for new phenomena in events with jets and missing transverse momentum in pp collisions at $\sqrt{s}$ = 13 TeV with the ATLAS detector*, Tech. Rep. ATLAS-CONF-2020-048 (CERN, Geneva, 2020).

[78] M. Cacciari, G. P. Salam, and G. Soyez, JHEP **0804**, 063 (2008), arXiv:0802.1189 [hep-ph].

[79] M. Cacciari, G. P. Salam, and G. Soyez, Eur. Phys. J. **C72**, 1896 (2012), arXiv:1111.6097 [hep-ph].

[80] G. Aad *et al.* (ATLAS), JINST **3**, S08003 (2008).

[81] G. Aad *et al.* (ATLAS), (2009), arXiv:0901.0512 [hep-ex].

[82] G. Aad *et al.* (ATLAS), Eur. Phys. J. C **79**, 970 (2019), arXiv:1907.05120 [hep-ex].

[83] *Expected performance of the ATLAS detector at the High-Luminosity LHC*, Tech. Rep. ATL-PHYS-PUB-2019-005 (CERN, Geneva, 2019).

[84] A. M. Sirunyan *et al.* (CMS), JHEP **06**, 027 (2018), arXiv:1801.08427 [hep-ex].

[85] M. Aaboud *et al.* (ATLAS), JHEP **05**, 041 (2019), arXiv:1812.09743 [hep-ex].

[86] M. Aaboud *et al.* (ATLAS), Phys. Rev. Lett. **120**, 211802 (2018), arXiv:1802.04329 [hep-ex].

[87] M. Aaboud *et al.* (ATLAS), JHEP **09**, 050 (2018), arXiv:1805.01649 [hep-ex].

[88] A. M. Sirunyan *et al.* (CMS), JHEP **03**, 131 (2020), arXiv:1912.01662 [hep-ex].

[89] M. Aaboud *et al.* (ATLAS), Phys. Rev. D **94**, 032005 (2016), arXiv:1604.07773 [hep-ex].

[90] M. Aaboud *et al.* (ATLAS), JHEP **01**, 126 (2018), arXiv:1711.03301 [hep-ex].

[91] A. M. Sirunyan *et al.* (CMS), JHEP **07**, 014 (2017), arXiv:1703.01651 [hep-ex].

[92] J. M. Lindert *et al.*, Eur. Phys. J. **C77**, 829 (2017), arXiv:1705.04664 [hep-ph].

[93] A. L. Read, *Advanced Statistical Techniques in Particle Physics. Proceedings, Conference, Durham, UK, March 18-22, 2002*, J. Phys. **G28**, 2693 (2002).

[94] L. Moneta, K. Belasco, K. S. Cranmer, S. Kreiss, A. Lazzaro, D. Piparo, G. Schott, W. Verkerke, and M. Wolf, *Proceedings, 13th International Workshop on Advanced computing and analysis techniques in physics research (ACAT2010)*, PoS **ACAT2010**, 057 (2010), arXiv:1009.1003 [physics.data-an].

[95] A. M. Sirunyan *et al.* (CMS), Phys. Rev. **D97**, 092005 (2018), arXiv:1712.02345 [hep-ex].